Determination of mechanical properties of biofilms by modelling the deformation measured using optical coherence tomography

Picioreanu, Cristian; Blauert, Florian; Horn, Harald; Wagner, Michael

DOI
10.1016/j.watres.2018.08.070

Publication date
2018

Document Version
Final published version

Published in
Water Research

Citation (APA)
Picioreanu, C., Blauert, F., Horn, H., & Wagner, M. (2018). Determination of mechanical properties of biofilms by modelling the deformation measured using optical coherence tomography. *Water Research*, *145*, 588-598. https://doi.org/10.1016/j.watres.2018.08.070

Water Research 145 (2018) 588–598

Contents lists available at ScienceDirect

Water Research

journal homepage: www.elsevier.com/locate/watres

Determination of mechanical properties of biofilms by modelling the deformation measured using optical coherence tomography

Cristian Picioreanu [a, *], Florian Blauert [b], Harald Horn [b], Michael Wagner [b]

[a] Department of Biotechnology, Faculty of Applied Sciences, Delft University of Technology, Delft, the Netherlands
[b] Water Chemistry and Water Technology, Engler-Bunte-Institut, Karlsruhe Institute of Technology, Karlsruhe, Germany

ARTICLE INFO

Article history:
Received 17 April 2018
Received in revised form
25 August 2018
Accepted 30 August 2018
Available online 1 September 2018

Keywords:
Biofilm mechanics
Elastic modulus
Poroelastic model
Fluid-structure interaction
Imaging

ABSTRACT

The advantage of using non-invasive imaging such as optical coherence tomography (OCT) to asses material properties from deformed biofilm geometries can be compromised by the assumptions made on fluid forces acting on the biofilm. This study developed a method for the determination of elastic properties of biofilms by modelling the biofilm deformation recorded by OCT imaging with poroelastic fluid-structure interaction computations. Two-dimensional biofilm geometries were extracted from OCT scans of non-deformed and deformed structures as a result of hydrodynamic loading. The biofilm geometries were implemented in a model coupling fluid dynamics with elastic solid mechanics and Darcy flow in the biofilm. The simulation results were compared with real deformed geometries and a fitting procedure allowed estimation of the Young's modulus in given flow conditions. The present method considerably improves the estimation of elastic moduli of biofilms grown in mini-fluidic rectangular channels. This superior prediction is based on the relaxation of several simplifying assumptions made in past studies: shear stress is not anymore taken constant over the biofilm surface, total stress including also pressure is accounted for, any biofilm shape can be used in the determinations, and non-linear behavior of mechanical properties can be estimated. Biofilm elastic moduli between 70 and 700 Pa were obtained and biofilm hardening at large applied stress due to increasing flow velocity was quantified. The work performed here opens the way for *in-situ* determination of other mechanical properties (e.g., viscoelastic properties, relaxation times, plastic yields) and provides data for modelling biofilm deformation and detachment with eventual applications in biofilm control and removal strategies.

1. Introduction

Formation of biofilms is regarded as a strategy of microbes to thrive in flowing environments and to protect themselves from environmental stresses by living attached to interfaces. Biofilms are aggregates of microorganisms (e.g., bacteria, algae, fungi) embedded in extracellular polymeric substances (EPS) (Flemming and Wingender, 2010). The EPS consist of a variety of proteins, polysaccharides and other substances, which form a hydrogel network stabilizing the biofilm structure and allowing the biofilm to withstand external stresses induced by the surrounding flow.

Beside the exact composition, structure and functions of the biofilm matrix, the mechanical properties of biofilms are still not entirely known. Currently, the biofilm mechanical properties cannot be predicted based on the acting microorganisms or growth conditions. Nevertheless, for water quality control in drinking water distribution systems (Shen et al., 2016) or for a reliable control of biofilm thickness in biofilm reactors (e.g., by backwashing of other mechanical methods) the knowledge of the mechanical stability would be extremely helpful (Morgenroth and Wilderer, 1999).

Guelon et al. (2011) provided a comprehensive overview of methods by which the mechanical properties of biofilms can be measured. Biofilm material can be subjected to *ex-situ* tests in well-known and standardized equipment (e.g., rheometers). However, developing *in-situ* measurement methods appears to be important as we do not know how quickly the mechanical properties might change if the biofilm is removed from its original environment (Guelon et al., 2011). A further review by Böl et al. (2013) related the available methods for identification of mechanical properties with the numerical modelling efforts. They concluded that none of the

* Corresponding author. Delft University of Technology, Department of Biotechnology, Van der Maasweg 9, 2629 HZ, Delft, the Netherlands.
E-mail address: c.picioreanu@tudelft.nl (C. Picioreanu).

https://doi.org/10.1016/j.watres.2018.08.070

existing methods by itself can cover the whole spectrum of biofilm behavior (Böl et al., 2013). Based on this statement, the combination of biofilm modelling together with in-situ experimental measurements of biofilm deformation could be a good approach to ascertain the mechanical properties of biofilms in their natural environment. For this aim, a fast and non-invasive imaging technique such as the optical coherence tomography (OCT) is required (Wagner and Horn, 2017).

Martin et al. (2014) used two-dimensional (2D) OCT cross-sections as a basis for the biofilm geometry, to assess by numerical modelling the permeation fluxes through membranes covered with patchy biofilms. Li et al. (2016) performed similar studies, using also 2D cross-sections from OCT. They could show that higher substrate fluxes were obtained for heterogeneous biofilm surface structures. Moreover, Fortunato et al. (2016) used OCT cross-sections to visualize biofouling in submerged membranes. They used the acquired imaging data to calculate the decrease in flux due to the biofouling and their theoretical estimations differed by only 5% from the original flux. A step forward was made by (Blauert et al., 2015), who managed to record 2D biofilm deformation in movies made with OCT. Confocal laser scanning microscopy (CLSM) was also combined with oscillatory shear rheology to measure the storage modulus G′ and loss modulus G″, connecting the G″ values to variations in EPS (Waters et al., 2014). Other authors used magnetic particles embedded in growing biofilms, which were manipulated by magnetic tweezers, generating a 3D map of mechanical biofilm properties (Galy et al., 2012).

Most of the numerical simulation studies aiming at describing dynamics of biofilm formation assumed the biofilm as a non-deformable, rigid material. Even when biofilm deformation and detachment were coupled with flow-induced stresses, the biofilm was assumed as an elastically deformable but quasi-static structure (Martin et al., 2015; Picioreanu et al., 2001; Radu et al., 2010). Several other studies combined the flow with biofilm deformation in a dynamic fashion (Tierra et al., 2015). The new possibility of simulating moving geometries allowed fluid-structure interaction biofilm models to describe, for example, oscillations of a biofilm streamers (Taherzadeh et al., 2010) and their effect on increased substrate uptake (Taherzadeh et al., 2012). The question is how the measured mechanical data can be combined with models. Typically, the fluid-structure interaction in biofilms is simulated with continuum approaches based on partial differential equations (e.g., finite element, finite volume, etc.) relying on published values of mechanical properties, such as Young's modulus and Poison's ratio (Taherzadeh et al., 2010). A finite element software (ANSYS) was used by Towler et al. to simulate the steady-state fluid structure interaction of a hemispherical biofilm structure in turbulent flow using a linear viscoelastic Burger constitutive relation for the biofilm material (Towler et al., 2006). Other authors applied a immersed boundary method to biofilm deformation simulated in a discrete approach based on particles connected by springs (e.g., Alpkvist and Klapper, 2007). Nevertheless, all numerical models need realistic values of biofilm properties (elastic, viscoelastic or plastic).

Within this study 2D images of deforming biofilms under defined flow conditions were used to derive biofilm mechanical properties by a series of numerical simulations mimicking the fluid-structure interaction. The biofilm imaging has been performed with OCT in micro fluidic flow channels (Blauert et al., 2015). This method proved several advantages, especially over CLSM imaging, for study of biofilm mechanics: it is non-invasive and in-situ, does not require staining, it can provide images at meso-scale (millimeters) and it is relatively fast.

2. Materials and methods

2.1. Biofilm cultivation

Biofilms were cultivated in flow cells made of poly(methylmethacrylate), with a straight channel of $2 \times 1 \times 124$ mm (width × height × length). The flow cells were inoculated with activated sludge supernatant from a local waste water treatment plant (KA Karlsruhe, Germany) for 24 h, before the supernatant was replaced by the cultivation medium.

Biofilm cultivation was performed with acetate (20 mg/L) or glucose (24 mg/L). The cultivation medium included one of the substrates together with nutrient and trace element solutions. The nutrient solution contained (concentrations in mg/L): K_2HPO_4 (2), $MgSO_4 \cdot 7H_2O$ (12), $Ca(NO_3)_2 \cdot 4H_2O$ (8), $(NH_4)SO_4$ (12) and $FeSO_4 \cdot 7H_2O$ (6). The trace element solution included (in μg/L): H_3BO_3 (300), $CoCl_2 \cdot 7H_2O$ (130), $CuCl_2$ (8), $MnSO_4 \cdot H_2O$ (20), $Na_2MoO_4 \cdot 2H_2O$ (26), $NiCl_2 \cdot 6H_2O$ (10) and $ZnSO_4 \cdot 7H_2O$ (56). The solution was phosphate buffered to pH = 7 and aerated to a dissolved oxygen concentration of ~8 mg/L.

Biofilms were cultivated at flow rates corresponding to Reynolds numbers ($Re = D_h\, u_{av}\, \rho/\mu$) from 11 to 472, calculated with measured average flow velocity u_{av}, water density ρ and viscosity μ, and hydraulic diameter $D_h = 2HW/(H+W)$ (1.33 mm) for the flow cell width W and height H. Biofilm development was followed by OCT (Blauert et al., 2015; Blauert, 2017).

2.2. Biofilm visualization and image processing

Imaging data-sets containing the biofilm geometry were acquired by means of optical coherence tomography (GANYMEDE I, Thorlabs GmbH, Lübeck, Germany). Briefly, OCT measures a point reflection signal from the biofilm and produces a depth-resolved intensity profile along the scan axis (z-direction, here the flow-cell height). By acquiring several scans along one lateral axis (x-direction, here the flow-cell length), a cross-sectional image is produced in the xz-plane. Consecutive cross-sections along the other lateral axis (the flow-cell width, y) generates a full volumetric representation, as detailed in (Haisch and Niessner, 2007; Wagner et al., 2010; Xi et al., 2006). OCT is suitable for *in-situ* biofilm imaging at the meso-scale (e.g., millimeter scale), no staining is required, it is non-invasive and acquires imaging data-sets fast. Cross-sections are obtained within milliseconds and full volumetric representations can be visualized within seconds. This allows OCT to follow fast processes over time either in “real time” (for 2-D cross-sections) or in time-lapsed mode (for 3-D volumetric representations).

For the mechanical study, cross-sections of $2 \times 1\ mm^2$ (1024×1024 pixels) were acquired, which corresponds to a resolution of 2 μm in the x direction and 2.9 μm in the z direction. The images were then cut to the area of interest, containing the biofilm structure. From these OCT images, the biofilm surface coordinates (x,z) were manually extracted with the free software Graph Data Extractor (A.J.Mattheuws). The list of points (x,z) was used to create polygonal shapes representing the biofilm geometry in the numerical simulations performed in COMSOL Multiphysics (COMSOL 5.3, Comsol Inc, Burlington, MA).

2.3. Shear induced biofilm deformation experiments

Experiments were carried out by step-wise changes in flow velocity and recording the corresponding biofilm deformation with OCT in a time-lapse series. Two recorded geometries were used for each biofilm: one at the unloaded geometry (no-flow = zero-shear) and the other at full (steady-state) deformation. Details can be

found in (Blauert et al., 2015). The acquired data-sets of the deformed and un-deformed structures were processed and loaded as model geometries into COMSOL Multiphysics for the numerical evaluation of mechanical properties.

2.4. Numerical model

2.4.1. Model geometry

The two-dimensional model in Fig. 1 presents an example of biofilm geometry (sub-domain Ω_B) extracted from OCT images, on which the fluid and solid mechanics calculations were based. The irregularly shaped biofilm sub-domain was placed in a rectangular box (length $L_x = 3$ mm and height $L_z = 1$ mm) representing an OCT cross-section of the flow cell along the flow direction. The difference between the outer rectangle and the biofilm sub-domain is the fluid sub-domain Ω_F.

2.4.2. Fluid and solid mechanics

The biofilm structure experiences the forces (shear and pressure) exerted by the moving liquid onto the biofilm surface (boundary Γ_{FSI} in Fig. 1). As a result, the biofilm deforms and this is experienced by the flow as a moving boundary, changing the flow pattern. This is a two-way interaction between the biofilm and the water flow, typically referred to as fluid-structure interaction (FSI). At the same time, inner cohesive forces prevent the biofilm from breaking apart and give rise to internal stresses.

Other processes which may issue internal forces (such as bacteria replication, motility, production of extracellular polymers or aging of the biofilm matrix) were neglected during the short time frame (seconds to minutes) in which the biofilm deformation was investigated. However, the pressure of water in the biofilm pores was taken into account in a poroelastic model formulation, counteracting the pressure exerted by the surrounding liquid. Pressure gradients in the deformable biofilm pores lead to a slow flow represented by Darcy's law.

Fluid flow outside the biofilm. Fluid flow in the sub-domain Ω_F was modeled by the incompressible laminar Navier-Stokes equations of momentum (1) and mass conservation (continuity) (2). The range of Re numbers investigated (up to 550) was well within the laminar flow regime in rectangular-section pipes.

$$\nabla \cdot \boldsymbol{\sigma}_F = \rho(\mathbf{u}_F \cdot \nabla)\,\mathbf{u}_F \tag{1}$$

$$\nabla \cdot \mathbf{u}_F = 0 \tag{2}$$

The liquid experiences pressure and viscous forces, included in the constitutive eq. (3) for the stress tensor $\boldsymbol{\sigma}_F$:

$$\boldsymbol{\sigma}_F = -p_F\mathbf{I} \;+\; \mu\left(\nabla\mathbf{u}_F + (\nabla\mathbf{u}_F)^T\right) \tag{3}$$

The variables solved for were the flow field velocity vector $\mathbf{u}_F$ and the liquid pressure p_F. Water density ρ and dynamic viscosity μ were assumed constant, with the values at 20 °C.

Solution of hydrodynamic equations involved the assumption that eventual biofilm structures upstream and downstream the imaged biofilm would be situated far enough not to affect the flow field in the studied domain. A fully-established laminar flow profile was imposed in the inflow Γ_i with an average velocity u_{av}. The outflow was set to a constant gauge pressure $p = 0$. On the channel walls (Γ_{wt} and Γ_{wb}) no-slip was imposed ($\mathbf{u}_F = 0$). On the FSI interface a "leaking wall" continuity condition was implemented with velocity taken from the Darcy flow within the biofilm, $\mathbf{u}_F = \mathbf{u}_B$.

Fluid flow in the biofilm. Darcy flow (4) with fluid mass conservation (5) was set in the biofilm sub-domain Ω_B:

$$\mathbf{u}_B = -\frac{\kappa}{\mu}\nabla p_B \tag{4}$$

$$\nabla \cdot \mathbf{u}_B = 0 \tag{5}$$

The gradient of pore liquid pressure p_B from the deformation of the porous structure relates with the liquid velocity u_B through the biofilm permeability κ (Coussy, 2004).

The no-flow condition $\partial p_B/\partial z = 0$ was applied on Γ_{wf}. The FSI interface assumed liquid continuity, coupling liquid pressure outside the biofilm with the pressure in biofilm pores, $p_F = p_B$.

Biofilm mechanics. The Navier equations for a solid in equilibrium, with quasi-static plane strain 2-D approximation (i.e., negligible small deformation out of the 2-D plane), were applied in the biofilm sub-domain Ω_B to represent the biofilm matrix deformation:

$$\nabla \cdot \boldsymbol{\sigma}_B = 0 \tag{6}$$

$$\nabla \cdot \mathbf{v}_B = 0 \tag{7}$$

Biofilms display elastic deformation in short stress exposure and viscous flow behavior during long stress exposure (Klapper et al., 2002; Shaw et al., 2004; Stoodley et al., 2002). In the experiments studied here the biofilm deformation occurred within seconds (with OCT B-scans acquired between 1 and 3 s from the flow change), which is much shorter than the expected transition time from elastic to viscoelastic deformation of ~20 min (Shaw et al., 2004). Therefore, viscous flow (creep) of the biofilm matrix was neglected and only the elastic behavior was considered. However,

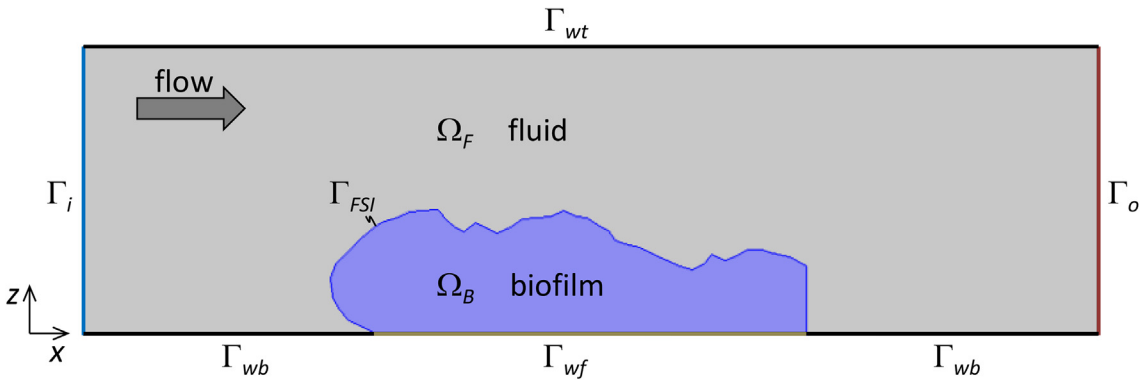

Fig. 1. Model domains and boundary conditions. Ω_F - water domain for fluid dynamics; Ω_B - biofilm domain in which the solid mechanics was calculated. Γ_{FSI} - fluid-structure interaction boundary with continuity of velocity and stresses; Γ_i - water inflow, fully-developed laminar flow of average velocity u_{av}; Γ_o - water outflow, zero gauge pressure; Γ_{wt}, Γ_{wb} - no-slip walls with zero flow velocity; Γ_{wf} - no-slip for flow and fixed solid structure for mechanics.

the porous nature of the biofilm cannot be overlooked for a correct representation of the fluid pressure in the biofilm matrix, which has to balance the pressure in the water domain. Therefore, the stress tensor in the biofilm included a poroelastic as well as an isotropic linear elastic component:

$$\boldsymbol{\sigma}_B = -\alpha\, p_B \mathbf{I} \;+\; \mathbf{C}(E,\nu) : \left(\nabla \mathbf{v}_B + (\nabla \mathbf{v}_B)^T\right)\Big/ 2 \qquad (8)$$

Replacing eq. (8) in (6), the variables solved for were the displacement field $\mathbf{v}_B$ and the fluid pressure inside biofilm pores p_B. The biofilm elasticity tensor $\mathbf{C}$ was expressed function of Young (elasticity) modulus E and Poisson ratio ν. The deformation field is directly influenced by the Young's modulus E, which can therefore be used as sensitive parameter in FSI models to fit the simulated deformation to the measured deformed geometry. The Poisson's ratio regulates thereby the lateral to the horizontal deformation. Additionally, the Biot-Willis coefficient α relates the volume change of fluid absorbed into, or released from the biofilm, to the volumetric change of the porous matrix. For soft porous materials $\alpha \approx 1$ (Coussy, 2004).

Continuity of total stress, $\boldsymbol{\sigma}_B = \boldsymbol{\sigma}_F$, was implemented on the FSI boundary as the load exerted by the flow of liquid on the biofilm surface. The biofilm was fixed on the support surface Γ_{wf}, with $\mathbf{v}_B = 0$.

Geometry deformation. equations (1)–(8) are shown here in the stationary form, because all the results presented in this study are based only on the computed deformation at steady-state compared with the OCT-recorded deformation. However, the steady-state solution was reached in time-dependent simulations, with the fluid-structure interaction coupled through a moving finite-element mesh. This was needed because preliminary simulations showed that not accounting for the reciprocal fluid-structure interaction (i.e. calculating the forces acting on the biofilm surface based only on the initial undeformed geometry) introduced errors in the biofilm deformation due to inaccurate load stress distributions.

Zero mesh displacement was prescribed on all boundaries, except on biofilm-liquid interface Γ_{FSI} where displacement was set to $\mathbf{v}_B$ by the solid mechanics.

2.4.3. Model solution

All model equations were implemented and solved in COMSOL Multiphysics 5.3 by a finite element method. Model parameters are listed in Table 1. A triangular mesh with maximum element size of 10 μm was used. Flow equations and the deformed geometry were discretized linearly, while quadratic discretization with geometric nonlinearity was applied for the solid mechanics. In time-dependent simulations, the flow velocity was increased from 0 to u_{av} in a smoothed step of 1 second. All results are reported at steady-state after 1.5 s.

2.4.4. Evaluation of Young's modulus E from the simulation

Parametric sweeps were performed with E from 50 to 800 Pa (depending on the experiment), to find the best overlap of the simulated and real deformed geometry recorded with OCT.

A first optimization criterion compared the non-overlapping area of model-computed biofilm deformation and experimental deformation (ΔA), relative to the area of experimental deformation (A_e), in percents $Err_a = \Delta A/A_e \times 100$. The model and experimental biofilm shapes were imported in COMSOL as solid polygonal shapes forming objects Ω_{Bm} and Ω_{Be}, respectively. The non-overlapping surface was found by a Boolean operation: $\Omega_{Bm} \cup \Omega_{Be} - \Omega_{Bm} \cap \Omega_{Be}$ (i.e., union minus intersection of the two shapes), as shown in Supplementary Information Fig. S1. Areas of non-overlapping surface and experimental biofilm were computed by surface integration.

Secondly, multiple parameter optimization was performed using the Nelder-Meed algorithm in MATLAB code coupled with COMSOL simulations (LiveLink for MATLAB). The objective function to be minimized was constructed as an average distance between points on the computed contour of deformed biofilm and the nearest polygonal segments forming the measured biofilm contour at deformed state (Err_m reported as μm error).

3. Results

3.1. Biofilm deformation measurements

The non-deformed biofilm geometry used as simulation basis was extracted from OCT images. Furthermore, OCT images taken for the deformed biofilms exposed to different flow conditions were compared with simulation results. Biofilm deformation experiments were adapted from (Blauert, 2017). Fig. 2a–c shows two-dimensional OCT cross-sections of a biofilm cultivated with glucose (case *Biofilm I*), taken over an area of $2000 \times 500\ \mu m^2$. A video of the deformation process was added in the Supplementary Information **SI V1**.

Supplementary video related to this article can be found at https://doi.org/10.1016/j.watres.2018.08.070.

Other biofilms cases were also investigated: *Biofilm II* and *Biofilm III* were grown with glucose, while *Biofilm IV* was cultivated with acetate. OCT images of non-deformed and deformed biofilm structures are presented in Fig. 3a–f.

3.2. Computed flow fields and stress distributions

Results from the numerical model simulation of fluid-biofilm interaction are presented in Fig. 4, at the stationary state reached after 1.5 s of time-dependent simulation (with inflow velocity increased during a smooth step of 1 s). The results are for the *Biofilm I* case at Re = 91, but similar solutions were obtained for the other biofilm cases and other Re numbers. The velocity field shows the expected laminar flow with larger fluid velocity above the biofilm obstruction (Fig. 4a). Due to the small biofilm permeability and small pressure gradients, much less flow establishes through the biofilm pores – with a Darcy velocity less than 1 μm/s (Fig. 4c). As a

Table 1
Model parameters.

Name	Description	Value	Units	Source
u_{av}	Average flow velocity	0 to 0.7	$m \cdot s^{-1}$	Experimental
ρ	Water density	1000	$kg \cdot m^{-3}$	Value at ~20 °C
μ	Water dynamic viscosity	0.001	$Pa \cdot s$	Value at ~20 °C
κ	Biofilm permeability	10^{-15}	m^2	(Dreszer et al., 2013)
α	Biofilm Biot-Willis coefficient	1	–	Assumed (soft material)
ν	Biofilm Poisson's ratio	0.4	–	Assumed as for gels (Geissler and Hecht, 1981)
E	Biofilm Young's modulus	70 to 700	Pa	Fitted (see Table 3)

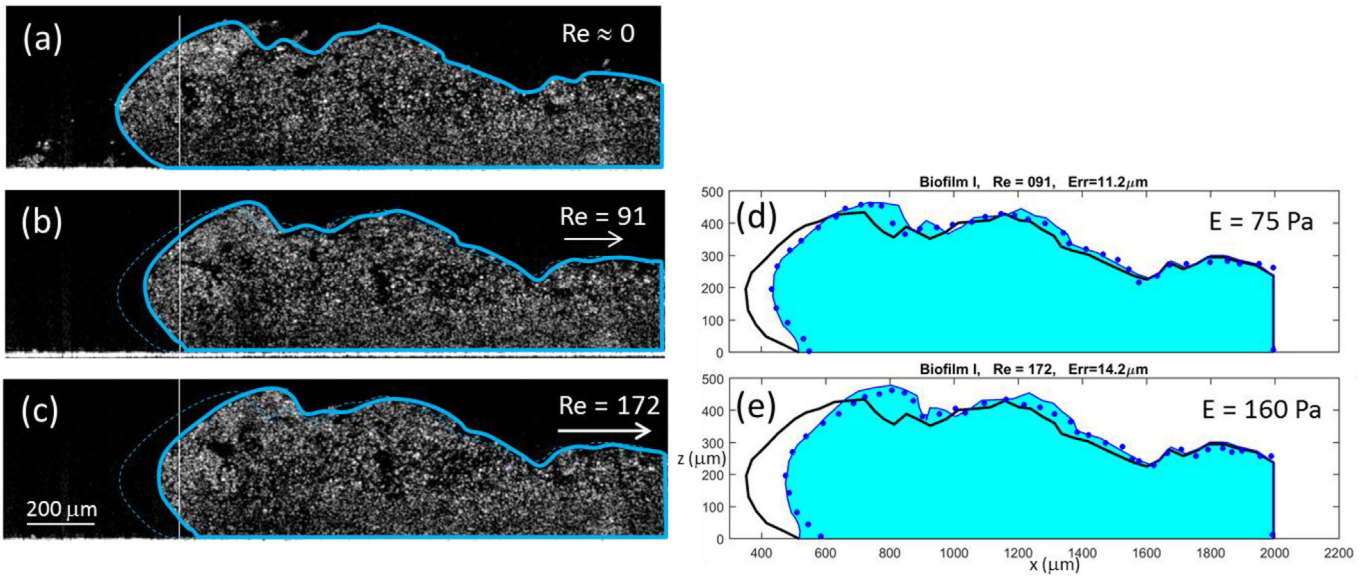

Fig. 2. **(a)**–**(c)**: OCT cross-section images of biofilms (case Biofilm I), unloaded (Re˜0) and loaded at different Re numbers, flow from left. Blue solid lines – biofilm contours providing geometry input in simulations (non-deformed at Re˜0) and compared with the simulation output (deformed at Re = 91 and Re = 172). Blue dashed lines – non-deformed biofilm contour. **(d),(e)**: Computed biofilm deformation compared with experimental measurements, for several biofilms at different Re numbers, as indicated on figure. Black lines - non-deformed structure; Blue dots - measured loaded (deformed) structure; Blue lines/shades - computed loaded structure; Error represents average deviation of computed biofilm shape from the measurements (in micrometers). (For interpretation of the references to color in this figure legend, the reader is referred to the Web version of this article.)

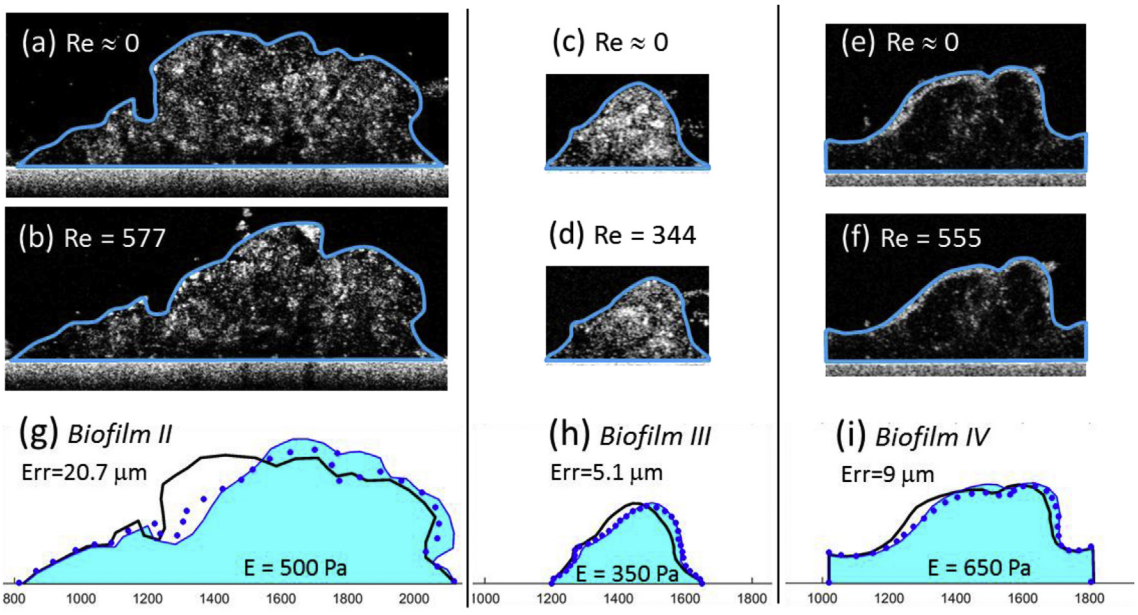

Fig. 3. **(a)**–**(f)**: OCT cross-section images of unloaded (Re˜0) and loaded biofilms at different Re numbers, with flow from left. **(a),(b)** Biofilm II (glucose medium); **(c),(d)** Biofilm III (glucose medium); **(e),(f)** Biofilm IV (acetate medium). Blue lines – biofilm contours from which geometry was extracted. **(g)**–**(i)**: Computed biofilm deformation compared with experimental measurements, for Biofilm II, III and IV at Re numbers indicated on figure. Black lines - unloaded (non-deformed) structure; Blue dots - measured loaded (deformed) structure; Blue lines/shades - computed loaded structure; Err_m in micrometers is average deviation of computed biofilm shape from the measurements. The same scale applies to all images as shown on the x-axis of model results (in μm). (For interpretation of the references to color in this figure legend, the reader is referred to the Web version of this article.)

result of the forces exerted by the flow, the biofilm deforms and reaches a stationary state. An animation of the time-dependent simulation is presented in Supplementary Information **SI V2**.

Supplementary video related to this article can be found at https://doi.org/10.1016/j.watres.2018.08.070.

The simulations considered the total stress applied along the bulk-biofilm interface Γ_{FSI}, that is both shear stress exerted tangentially on the biofilm surface by the viscous flow and pressure acting normally to the biofilm. The total stress distributions in Fig. 4b present values from close to zero to a maximum of 12 Pa (or N/m^2). It becomes clear that the pressure dominates on the biofilm frontally exposed to flow, exerting a compressive load (i.e., pushing the biofilm inwards). Conversely, on the biofilm top the negative pressure exerted a tensile load (i.e., traction) pulling the biofilm outwards. Interestingly, the pressure (max. 9 Pa) is larger than the shear stress (max. 3 Pa), as compared in Fig. 4c. The shear was

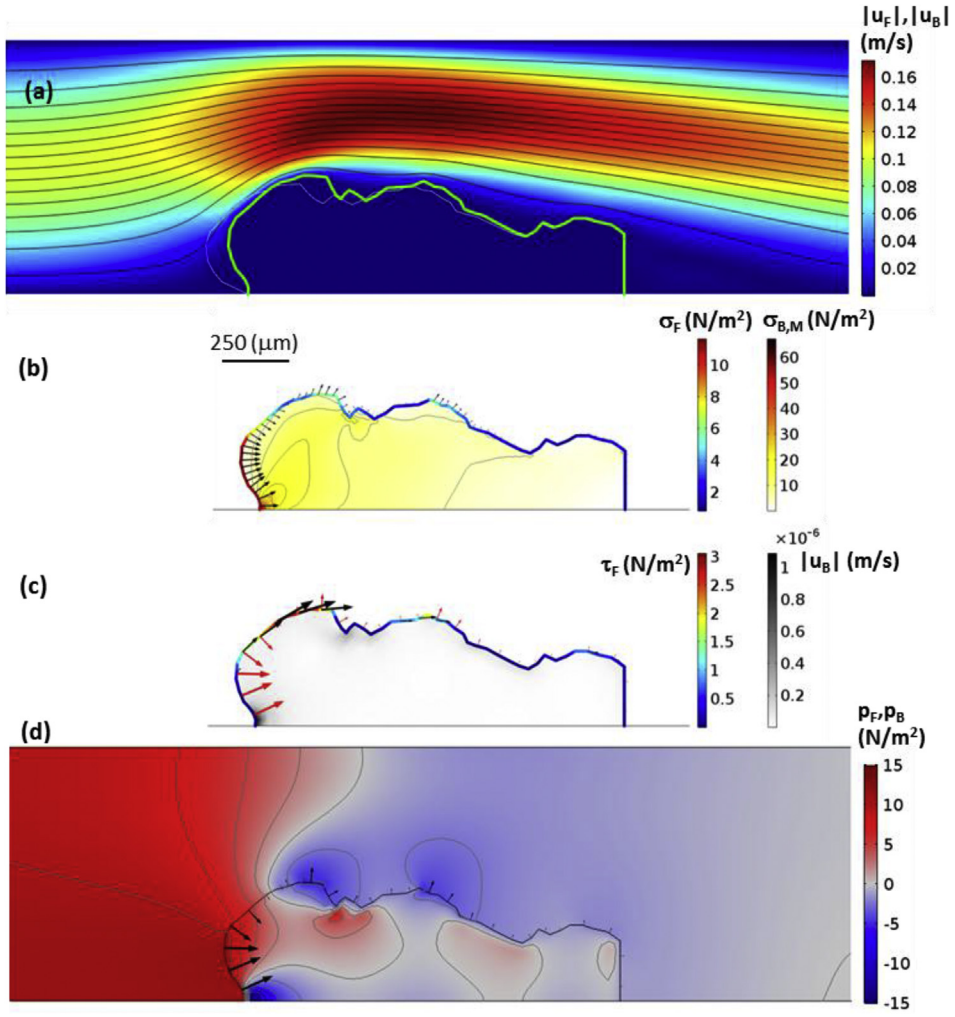

Fig. 4. Numerical model results for Biofilm I case at Re = 91, in the stationary state. **(a)** Liquid velocity distributions outside biofilm (laminar flow) and inside biofilm (Darcy flow), with liquid streamlines (black curves). White line: non-deformed biofilm shape; Green line: fully deformed biofilm shape. **(b)** Total fluid stress exerted on the biofilm structure σ_F (arrows and colored contour) and Von Mises stress in the biofilm $\sigma_{B,M}$ (colored surface). **(c)** Viscous (shear) fluid stress on the biofilm structure τ_F (black arrows and colored contour), fluid pressure on the biofilm (red arrows at scale 1:5 relative to shear stress), and Darcy velocity magnitude in the biofilm $|\mathbf{u}_B|$ (colored surface). **(d)** Fluid pressure outside/inside the biofilm (colored surface) and on the biofilm structure (arrows). (For interpretation of the references to color in this figure legend, the reader is referred to the Web version of this article.)

found to act mainly on the up-front biofilm surface, in the rest being much smaller than the pressure. Slightly increased friction was only on the high points in the middle of the biofilm structure. This shows that the tested biofilm was mainly compressed from the upstream side, and experienced a small drag along the whole structure due to the shear forces.

The forces on the biofilm surface produce mechanical stress non-uniformly distributed in the biofilm (Fig. 4b). The von Mises stress reduces the local stress in all directions to one scalar value, making it easier to compare the local stress to a failure criterion, for which the material would break. Naturally, the fluid forces exerted on the biofilm front coincide with the largest deformation and largest internal stresses in this region. Simulation showed the highest stresses close to the upstream contact point of biofilm and substratum ("hinge" effect), where the main deformation would occur were the biofilm not firmly attached to substratum. However, comparison of the computed deformation in the hinge area with the collected OCT images is not easy. The apparent gliding effect of the biofilm base at higher Re flows (Fig. 2b and c) was not considered in the simulations, which assumed the whole biofilm base fixed to the support (Fig. 2d and e and Fig. 4).

3.3. Assessment of the elastic modulus E

The evaluation of material elastic modulus was done by performing a parametric sweep over a range of *E* values to find the best fit for the computed deformation to the measured deformed biofilm geometry. While in conventional FSI simulations the model is set with known mechanical parameters and the desired output is the deformed geometry, in this study the method can be seen as reversed: the deformed geometry was used to assess values of the mechanical properties.

As an example, for the *Biofilm I* changing the elastic modulus resulted in important geometry changes upon flow at Re = 172 (Fig. 5a). As expected, large deformations occur at smaller values of *E*. While compression occurs on the biofilm frontal zone, traction takes place on the upper biofilm sections. A value of *E* around 160 Pa was found to fit best the measured deformed biofilm contour, with an error of 14 μm in average (Fig. 2e). At the lower Re = 91, the elastic modulus best fitting the recorded structure deformation was ~80 Pa, with $Err_m = 11$ μm and $Err_a = 3.5\%$, as displayed in Fig. 2d. Table 2 lists the model/measurement differences for the parametric sweep of the Young's modulus from 50 to

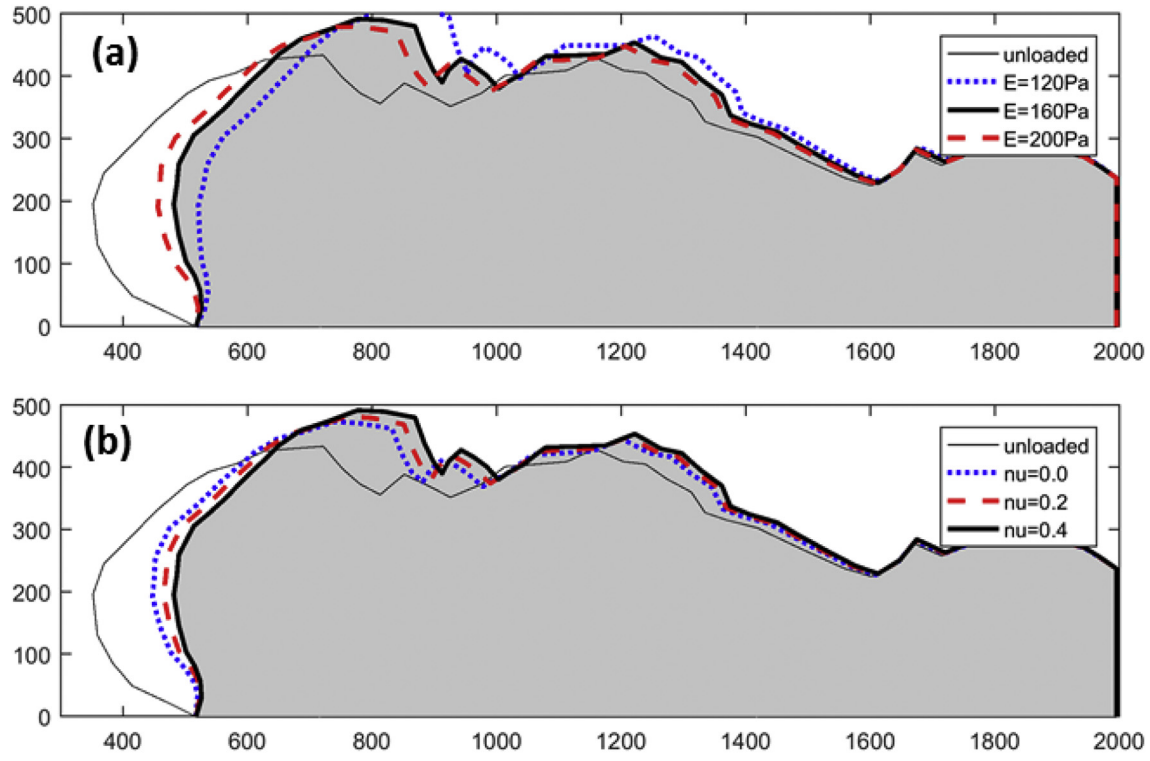

Fig. 5. Computed deformation of Biofilm I at Re = 91 in a series of parameter sweeps with: (a) elastic modulus E (at $\nu = 0.4$) and (b) Poisson ratio ν (at $E = 160$ Pa). Other model parameters as in Table 1. The grey-shaded area represents the deformed biofilm geometry calculated with the reference values.

120 Pa. Smaller E lead to a rapid degradation of the fit as the structure deforms too much. Both error measures lead to the same conclusions. Given the strong 2-D simplification, the model comes remarkably close to the real deformation. The simulated displacement field is in good agreement with the shear stress distribution, showing that the largest displacement is in the upper front region. The main deformations always occur in the frontal region of the biofilm, this being also the most difficult part to model correctly. For the simulations a Poisson ratio of $\nu = 0.4$ was chosen, in similarity with gels (Geissler and Hecht, 1981) and with theoretical estimations by (Laspidou and Aravas, 2007), due to lack of other experiments. The Poisson's ratio relates the lateral to transverse elongation during the deformation process, influencing the deformation field within the biofilm matrix. Parametric sweeps with the Poisson ratio reveal that the simulated biofilm structure sinks as lower values are chosen (Fig. 5b), while keeping the same E. However, the choice of a conservative value of $\nu = 0.4$ results in good fits, not only for *Biofilm I* but also for the other cases (Fig. 3). Simulations with different values of Biot parameter α and biofilm permeability κ showed practically no model sensitivity within an acceptable range of values (α between 1 and biofilm porosity of 0.6; κ changed by two orders of magnitude, see SI Fig. S3).

Table 2
The differences between Biofilm I deformed geometry as measured and calculated, at Re = 91.

Elastic modulus E [Pa]	Average distance error Err_m [μm]	Overlap area error Err_a [%]
50	19.9	8.0
60	14.8	5.6
70	11.6	4.1
80	*10.9*	*3.5*
90	11.1	3.8
100	11.5	4.0
110	11.7	4.3
120	12.1	4.6

In addition to *Biofilm I*, other biofilm structures were examined: glucose-grown *Biofilms II and III* and acetate-grown *Biofilm IV*. The simulated and measured biofilm deformations are summarized in Fig. 3, while all tests and conditions reported here are listed in Table 3. Overall, the agreement between the measured and computed deformations was good. Simpler biofilm shapes and smaller biofilm areas seem to lead to better results (*Biofilm III*, $Err_m = 5$ μm and *Biofilm IV*, $Err_m = 9$ μm). The obtained E values for these biofilms appear notably higher than for *Biofilm I*, however, these deformations were performed at larger Re numbers where due to larger forces biofilm hardening effects occur. Notably more than for *Biofilm I*, the pressure dominates over the shear stress in *Biofilm III* that has a dome-like shape (Fig. 6). Large pressure pushes the biofilm downstream and pulls it upward (max. ~30 Pa), while the shear increases as expected over the biofilm height but displays much lower values (max. 10 Pa at the biofilm top). This reflects once again the importance of considering correct hydrodynamic representation of forces, not only an overall shear such as in previous studies. A firm base leads to a more uniform von Mises stress distribution within *Biofilm III* compared with *Biofilm I*.

3.4. Biofilm hardening and consolidation

Experimental techniques often evaluate a single value of the elastic modulus for biofilms, assuming that this value is valid over a large range of elastic deformations (Möhle et al., 2007; Stoodley et al., 1999). Laspidou and Aravas (2007) predicted that the value of Young's modulus can be influenced by the change of porosity during deformation. As a result, biofilm consolidation occurs (i.e., closing or collapsing of voids), which leads to an increase of the elastic modulus. This biofilm hardening effect was observed

Table 3
Overview of biofilm deformation tests and conditions.

Name	Substrate concentration and Reynolds number during growth	Reynolds number at deformation, Re (–)	Estimated elastic modulus, E (N/m^2)	Fitting error Err_m (μm)
Biofilm I	Glucose 30 mg/L, Re = 4	91	75	11.2
		172	160	14.2
Biofilm II	Glucose 24 mg/L, Re = 55	577	500	20.7
Biofilm III	Glucose 24 mg/L, Re = 55	344	350	5.1
Biofilm IV	Acetate 20 mg/L, Re = 11	555	650	9
Biofilm V	Glucose 30 mg/L, Re = 4	238	70	23
		477	190	32
		477	40 to 900 (variable)	15

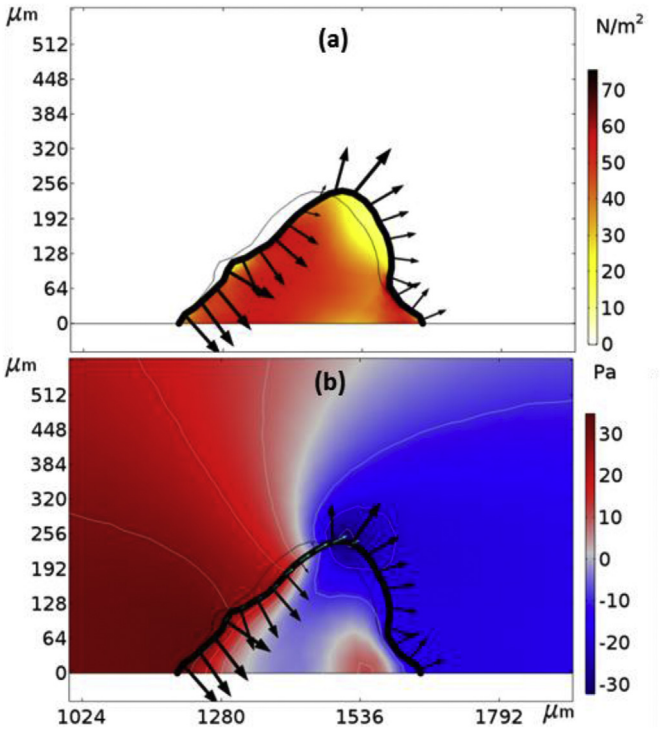

Fig. 6. Model results for Biofilm III at Re = 344 with E = 350 Pa. **(a)** Total fluid stress on the biofilm σ_F (black arrows) and Von Mises stress in the biofilm $\sigma_{B,M}$ (colored surface). **(b)** Fluid pressure outside and inside the biofilm (colored surface); Fluid pressure acting on the biofilm (black arrows, normal to surface) compared with a much smaller shear (light blue arrows, tangential to surface). Thick black line: deformed biofilm structure; Thin black line: initial (non-deformed) biofilm. (For interpretation of the references to color in this figure legend, the reader is referred to the Web version of this article.)

experimentally by (Paramonova et al., 2009) in *Streptococcus* dental biofilms. However, experimental data for biofilm hardening ("stiffening") are still scarce and coupling *in-situ* OCT imaging with numerical modelling of biofilm deformation under a range of flow velocities could contribute to the quantification of this effect. Recently, biofilm hardening at large stresses has been observed for biofilms formed in gravity-driven filtration, upon applied step-wise changes in permeate flux or trans-membrane pressure (Jafari et al., 2018). In addition to hardening, biofilm consolidation has also been reported (Alpkvist et al., 2006), meaning that the biofilm base becomes denser in time. The increase of biofilm density toward the support was experimentally evaluated in several studies (e.g., Zhang and Bishop, 1994). However, whether this also leads to increased biofilm stiffness (i.e., with increased E compared with the upper "younger" biofilm layers) still remains to be measured. The hardening effect is evident in the experiments with *Biofilm I*. The Young's modulus evaluated at Re = 91 was ~80 Pa, while at Re = 172 a value of ~160 Pa was found to fit best the data. When applying the E = 80 Pa for Re = 172 case, unrealistically large deformations were calculated.

The biofilm hardening and consolidation were also measured in a separate biofilm case, *Biofilm V*, as shown in Fig. 7. For this biofilm grown on glucose, deformations were recorded at Re = 238 and Re = 477 and the best deformed geometry fits were obtained with E = 70 and 190 Pa, respectively. This shows that the biofilms get harder at larger flow velocity (i.e., more applied stress on the biofilm) (Fig. 7a and b). However, the match is not very good, especially at the larger Re, were both the frontal surface and the back of the biofilm deviate from the observed deformation. It is clear that the real biofilm deformed less close to the base and more at the top surface, than the model with uniform E would predict. Therefore, we have also imposed an elasticity profile with larger E at the base and much smaller at the top, as shown in Fig. 7c and d. While for the slow flow the match did not improve, for the fast flow (Re = 477) the model-computed biofilm deformation fitted better the measurements. Visibly, the frontal region close to base deforms less, while the top region deforms more (Fig. 7d). No attempt was made to further tune the imposed elasticity profile, as for that more local deformation measurements would be needed – possibly by tracking the displacement of marked biofilm points. These poroelastic simulations show how gradients in biofilm elasticity can explain consolidation effects near the support, but also how biofilm compression can be achieved without changing the Poisson's ratio. However, it can not be excluded that the studied biofilms were also deformed plastically, i.e. upon flow rate increase the structure suffered some permanent deformation. This would be certainly possible by closing macropores and collapsing the finger-like structures often seen at the biofilm surface into a more compact structure.

4. Discussion

4.1. Stress in the biofilm

Simulations performed in this study showed invariably high stresses within the biofilm frontal section, close to the attachment surface. Similar stress distributions in biofilms were found by Taherzadeh et al. (2012), who simulated oscillatory biofilm streamer movements. The shear stress decreases along the tail of the streamer, indicating a phenomenological advantage of the streamlined structure in fast flows. Böl et al. (2009) used a biofilm geometry obtained from confocal laser scanning images for

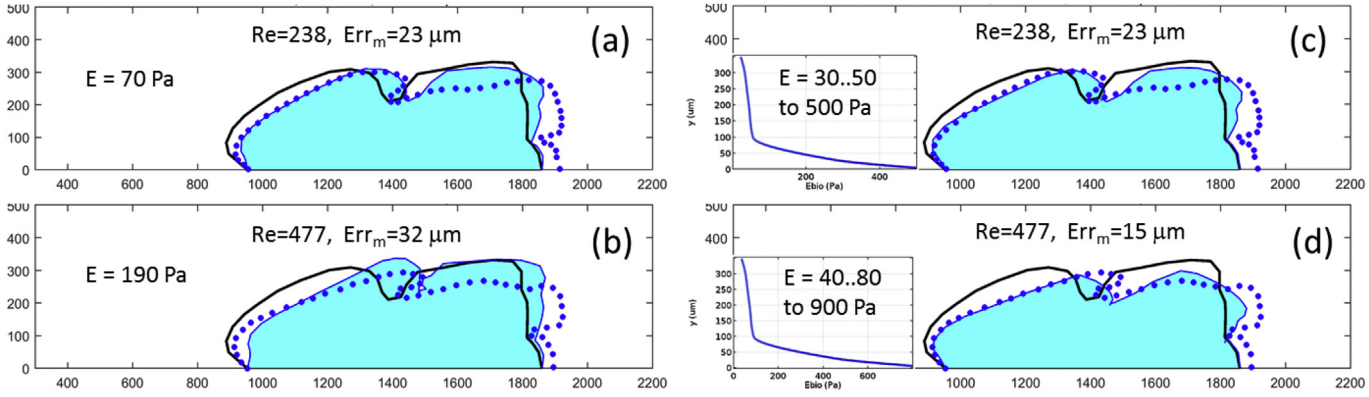

Fig. 7. Computed Biofilm V deformation compared with experimental measurements at Re 238 and 477. **(a),(b)** Uniform elastic modulus in the biofilm; **(c),(d)** Distributed elastic modulus in a consolidated biofilm. The inserts show the assumed E variation over the biofilm height. Black lines - unloaded structure; Blue dots - measured loaded structure; Blue lines/fill - computed loaded structure; Error represents average deviation of computed biofilm shape from the measurements (in μm). (For interpretation of the references to color in this figure legend, the reader is referred to the Web version of this article.)

simulation of the fluid-structure interaction. Their work provided similar results to those presented here, showing the highest inner stresses around the bended biofilm "neckings". This also points to the importance of using real biofilm geometries, such those in Figs. 2 and 3, for obtaining a more accurate picture of the shear stress distribution within the biofilm. Moreover, this weak contact point is a possible place where the biofilm detachment begins. Picioreanu et al. (2001) studied in a 2D simulation the influence of shear stress on the detachment behavior of biofilms. Even though the simulations were based stong simplifing assumptions (biofilm as homogeneous elastic material), they showed the importance of stress distribution on and within the biofilm structure in determining areas of large deformation, as well as regions prone to detachment. Moreover, this created the base for model extensions to multispecies biofilms (Martin et al., 2015), bioclogging of porous media (Bottero et al., 2013), or biofouling of membrane filtration devices (Radu et al., 2010). The method developed in the present study could therefore provide very useful information (both input parameters and data to check model output) for more elaborate modelling of biofilm detachment.

A comparison of elastic modulus *E* obtained in this study with values resulting from other studies is only qualitatively possible. The *E* moduli in this study ranged from 70 to 700 Pa (Table 3). The values are slightly larger than other experimentally determined Young's moduli from flow cell setups: 40 Pa in mixed cultures (Stoodley et al., 1999; Blauert et al., 2015), 20–250 Pa for *P. aeruginosa* (Stoodley et al 1999, 2001; Klapper et al., 2002). Other tests of the mechanical strength of biofilms, such as compression measurements, were used by Paramonova et al. (2009), yielding values closer to this study (E = 50–350 Pa). However, direct comparison to other techniques (compression, indentation, atomic force microscopy, shear rheometry, etc.) is difficult, as long as standardized samples and test conditions do not exist.

4.2. Importance of shear and pressure exerted by the fluid

Model results clearly showed that the tested biofilms were mostly compressed upstream and experienced only relatively small shear. These findings have actually profound implications on the validity of results obtained in other studies (Blauert et al., 2015; Stoodley et al., 1999) considering only the shear stress in the determination of the elastic modulus. The underestimation of forces acting on a biofilm for which a certain deformation was measured would lead to underestimation of the biofilm stiffness. Moreover, the same value of shear was assumed to act uniformly on the whole biofilm surface in previous studies. Critically, these studies took the shear estimated from the liquid velocity in the empty channel in the calculation of mechanical moduli, whereas the biofilm could obstruct an important flow section resulting actually in larger shear. For example, a shear value $\tau = 0.3$ Pa was used in Blauert et al. (2015) for the same *Biofilm I* at Re 90, while in the present study an average shear $\tau = 0.66$ Pa was calculated on the biofilm surface, with large local variations from ~0 to 3 Pa. Moreover, the total stress (including pressure) was $\sigma = 4.1$ Pa, which clearly shows that the estimation of the Young's modulus relies on a good assumption of the forces responsible for the deformation. Considering the shear only can underestimate the actual total stress and therefore the real Young's modulus of the biofilm. Using the newly developed fluid-biofilm interaction model we relaxed the assumption of a constant shear stress, revealing a more realistic value for the Young's modulus.

In past studies, the elastic (Young's) modulus was experimentally evaluated from the linear part of a stress-strain plot based on images of biofilm deformation at different shear stress (Blauert et al., 2015; Böl et al., 2013; Stoodley et al., 1999). This method requires a certain shape of the biofilm structure and introduces errors from manual calculation of the shear stress and strain. For example, biofilms had to present a straight edge and certain "attack angles" of the section facing the flow to allow determination of shear modulus, or large finger-like structures to calculate the Young's modulus from elongation measurements. Implementing a real biofilm geometry into a numerical simulation should also allow the determination of mechanical parameters from any biofilm geometries.

Considering the coupled fluid-biofilm interaction instead of computing deformation based on the forces exerted only on the underformed structure has a certain effect. For the coupled model, the average total stress over the whole bulk-biofilm boundary was $\sigma = 4.1$ Pa and the average shear stress $\tau = 0.66$ Pa. In a decoupled case, when biofilm deformation did not affect the flow, $\sigma = 3.56$ Pa and $\tau = 0.64$ Pa. This simplification introduces another possible source of errors in the deformation forces. The computed biofilm deformation in this case showed indeed less compression and a biofilm pulled slightly more upwards (SI Fig. S2).

4.3. Biofilm hardening, porosity and compressibility

Assuming Poisson's ratios close 0.5 imply that the structure would be nearly incompressible, requiring that biofilms maintain volume while deforming. However, in some cases, OCT imaging of

deformation showed that biofilm compression occurs. This could be mainly attributed to pressure forces. It has also been shown that during the deformation at higher flow velocities the porosity decreases (Blauert et al., 2015). Water extrusion from the biofilm makes the structure more rigid. Several empirical formulae have been proposed to describe the dependence of mechanical strength on porosity ϕ. For example, for ceramic materials $E = E_0(1\text{-}\phi/\phi_{crit})^n$ (Phani and Niyogi, 1987) implies the existence of a critical porosity at which the Young modulus becomes zero, or $E = E_0\exp(\text{-}m\phi)$ was proposed for porous sintered materials (Ryshkewitch, 1953). Recently, a simple power-law $E = E_0\phi^{-m}$ was used to describe biofilm hardening in gravity-driven filtration (Jafari et al., 2018), related to compression under pressure or due to flow-induced internal friction. Additionally, re-arrangement of polysaccharides and polypeptides may also play a role in biofilm stiffening, especially when the shear stress is applied longer than viscoelastic relaxation times (~minutes) (Shaw et al., 2004).

The results of this study are in agreement with the theoretical estimations of elastic modulus change with decreasing porosity by (Laspidou and Aravas, 2007). In their model the decrease in porosity at least doubled the Young's modulus, while a similar trend was found in our study. Moreover, Laspidou and Aravas showed that by assuming a compressible or incompressible biofilm material, the slope of both Young's modulus and Poisson's ratio with the strain can also be altered. Unfortunately, the OCT imaging alone does not reveal mechanical heterogeneity of the biofilm. OCT might well be used to reveal denser regions inside the structure to include heterogeneity in future calculations. It may also be possible to couple particle tracking techniques with OCT to determine deformation fields and from this to estimate the spatial heterogeneity of mechanical properties within the biofilm.

4.4. Sources of errors in the OCT/model determination of mechanical properties

Several factors that may compromise the accuracy of determination of elastic properties by coupling OCT imaging with numerical modelling have been already discussed. These included non-elastic behaviors (viscoelastic or plastic), non-linear elasticity with biofilm hardening at high applied loads and compression with porosity change (e.g., biofilm porosity decrease up to 10% (Blauert et al., 2015) has a hardening effect), mechanical consolidation of base layers, or other factors leading to heterogeneous distribution of properties (e.g., if bacteria tend to build clusters, regions of locally stiffer or softer biofilm can develop). Other possible interferring factors are discussed here.

Steady-state deformation not achieved. This could be caused by viscoelastic biofilm behavior, which keeps deforming even when the shear stress exerted by the liquid reached a quasi-constant value. This continuous deformation should however be minimal in the present study, because the acquisition time was long enough compared with the viscoelastic time constants (seconds) measured by other researchers (Peterson et al., 2013) and still short compared with the time scale of long-term macromolecular rearrangements (~20 min) (Klapper et al., 2002; Shaw et al., 2004). In addition, it could be noted that the biofilm imaged in the Supplementary Information **SI V1** vibrated slightly under flow with an amplitude of ~10 μm. The assumed steady deformation should therefore be considered within this marge of error.

Changes in the flow pattern. Typically, the flow established very fast (seconds) in the performed experiments and the volumetric flowrate was accurately measured. However, the average velocity value calculated in the simulations from the volumetric flowrate may be altered by variations in the crossectional area. Higher velocities and shear stress may be caused by biofilm patches not removed by regular cleaning, growing on the upper and lateral flowcell walls, which decrease the flow section. The flow pattern could also be affected by biofilm colonies growing upstream the observed biofilm patch (and much less by those downstream, which can only affect the recirculation vortex behind the obstacle in the flow). We used here fully-developed laminar flow in inlet with an average velocity corresponding to measured volumetric flowrate – this excluding influences by other upstream obstacles on the flow pattern. However, if other biofilm colonies are placed upstream, the water velocity near the biofilm base will be slower, recirculation zones will occur and the forces upon the biofilm base will be smaller. This could eventally be approximated by a periodic flow condition applied to inlet and outlet flow boundaries (as if, the observed biofilm colony would repeat periodically) (e.g., Haaksman et al., 2017).

Three-dimensional effects. These could arise from biofilm deformation in the out-of-plane direction y, not considered in the plain-strain mechanical model as neither 3-D flow components were considered. Certainly, for an accurate evaluation of the biofilm mechanical properties, volumetric biofilm deformations should be acquired by OCT and then interpreted by a full 3-D fluid-structure interaction model. The difficulty however is not only a strongly increased computing time and memory, but more importantly the integration of the OCT image into the computational model. Surface smoothing, noise removal and advanced image thresholding would be needed to construct a meshable 3-D object. Nevertheless, such techniques exist, for example developed when importing 3-D CT scans of complex structures into CFD models (Haaksman et al., 2017). In extension, we believe that the methodology developed here could also be applied in flow cells or channels with non-rectangular geometry or irregular walls. However, the requirement of an optical window allowing for the visualization by means of OCT remains.

Biofilm erosion and detachment. These could affect the recorded biofilm shape at high Re numbers. It cannot be excluded that the slight biofilm compression observed at high flow rates could also be due to surface erosion (i.e., loss of biofilm material as a result of fluid shear forces).

5. Conclusions

This study developed a method for the determination of elastic properties of biofilms by modelling the biofilm deformation recorded in 2-D slices by optical coherence tomography imaging with poroelastic fluid-structure interaction numerical computations. The present method considerably improves the estimation of elastic moduli of biofilms grown in mini-fluidic rectangular channels. This improved prediction is based on the relaxation of several simplifying assumptions made in past studies: shear stress is not anymore taken constant over the biofilm surface, total stress including also pressure is accounted for, any biofilm shape can be practically used in the determinations, and non-linear behavior of mechanical properties can be estimated. Biofilm elastic moduli between 70 and 700 Pa were obtained and biofilm hardening at large applied stress due to increasing flow velocity was quantified. The work performed here opens the way for *in-situ* determination of other mechanical properties (Poisson ratio, viscoelastic modulus and relaxation time, plastic yields, etc.). Furthermore this provides data for modelling of biofilm deformation and detachment with eventual applications in biofilm control and removal strategies.

Acknowledgements

This work was funded by the European Commission grant 611640. The research of Michael Wagner and Harald Horn is

supported by the German Research Foundation (DFG HO 1910/16-1). The authors thank Juan-Pablo Pavissich from Universidad Adolfo Ibáñez (Viña del Mar, Chile) for work performed in the early stages of this project.

Appendix A. Supplementary data

Supplementary data related to this article can be found at https://doi.org/10.1016/j.watres.2018.08.070.

References

Alpkvist, E., Picioreanu, C., Van Loosdrecht, M.C.M., Heyden, A., 2006. Three-dimensional biofilm model with individual cells and continuum EPS matrix. Biotechnol. Bioeng. 94, 961–979.

Alpkvist, E., Klapper, I., 2007. Description of mechanical response including detachment using a novel particle model of biofilm/flow interaction. Water Sci. Technol. 55, 265–273.

Blauert, F., 2017. Investigating Biofilm Deformation Using Optical Coherence Tomography and Fluid-structure Interaction Simulation. PhD Thesis. Karlsruhe Institute of Technology.

Blauert, F., Horn, H., Wagner, M., 2015. Time-resolved biofilm deformation measurements using optical coherence tomography. Biotechnol. Bioeng. 112, 1893–1905.

Bottero, S., Storck, T., Heimovaara, T.J., Van Loosdrecht, M.C.M., Enzien, M.V., Picioreanu, C., 2013. Biofilm development and the dynamics of preferential flow paths in porous media. Biofouling 29 (9), 1069–1086.

Böl, M., Ehret, A.E., Bolea Albero, A., Hellriegel, J., Krull, R., 2013. Recent advances in mechanical characterisation of biofilm and their significance for material modelling. Crit. Rev. Biotechnol. 33, 145–171.

Böl, M., Möhle, R.B., Haesner, M., Neu, T.R., Horn, H., Krull, R., 2009. 3D finite element model of biofilm detachment using real biofilm structures from CLSM data. Biotechnol. Bioeng. 103, 177–186.

Coussy, O., 2004. Poromechanics. John Wiley & Sons, Ltd, Chichester, UK.

Dreszer, C., Vrouwenvelder, J.S., Paulitsch-Fuchs, A.H., Zwijnenburg, A., Kruithof, J.C., Flemming, H.C., 2013. Hydraulic resistance of biofilms. J. Membr. Sci. 429, 436–447.

Flemming, H.-C., Wingender, J., 2010. The biofilm matrix. Nat. Rev. Microbiol. 8, 623–633.

Fortunato, L., Qamar, A., Wang, Y., Jeong, S., Leiknes, T., 2016. In-situ assessment of biofilm formation in submerged membrane system using optical coherence tomography and computational fluid dynamics. J. Membr. Sci. 521, 84–94.

Galy, O., Latour-Lambert, P., Zrelli, K., Ghigo, J.-M., Beloin, C., Henry, N., 2012. Mapping of bacterial biofilm local mechanics by magnetic microparticle actuation. Biophys. J. 103 (6), 1400–1408.

Geissler, E., Hecht, A.M., 1981. The Poisson ratio in polymer gels. 2. Macromolecules 14, 185–188.

Guelon, T., Mathias, J.D., Stoodley, P., 2011. Advances in Biofilm Mechanics. Springer, Berlin.

Haaksman, V.A., Siddiqui, A., Schellenberg, C., Kidwell, J., Vrouwenvelder, J.S., Picioreanu, C., 2017. Characterization of feed channel spacer performance using geometries obtained by X-ray computed tomography. J. Membr. Sci. 522, 124–139.

Haisch, C., Niessner, R., 2007. Visualisation of transient processes in biofilms by optical coherence tomography. Water Res. 41, 2467–2472.

Jafari, M., Desmond, P., Van Loosdrecht, M.C.M., Derlon, N., Morgenroth, E., Picioreanu, C., 2018. Effect of Biofilm Structural Deformation on the Hydraulic Resistance in Ultrafiltration: A Numerical and Experimental Study. Water Res. 145, 375–387.

Klapper, I., Rupp, C.J., Cargo, R., Purvedorj, B., Stoodley, P., 2002. Viscoelastic fluid description of bacterial biofilm material properties. Biotechnol. Bioeng. 80, 289–296.

Laspidou, C.S., Aravas, N., 2007. Variation in the mechanical properties of a porous multi-phase biofilm under compression due to void closure. Water Sci. Technol. 55, 447–453.

Li, C., Felz, S., Wagner, M., Lackner, S., Horn, H., 2016. Investigating biofilm structure developing on carriers from lab-scale moving bed biofilm reactors based on light microscopy and optical coherence tomography. Bioresour. Technol. 200, 128–136.

Martin, K.J., Bolster, D., Derlon, N., Morgenroth, E., Nerenberg, R., 2014. Effect of fouling layer spatial distribution on permeate flux: a theoretical and experimental study. J. Membr. Sci. 471, 130–137.

Martin, K.J., Picioreanu, C., Nerenberg, R., 2015. Assessing microbial competition in a hydrogen-based membrane biofilm reactor (MBfR) using multidimensional modeling. Biotechnol. Bioeng. 112, 1843–1853.

Möhle, R.B., Langemann, T., Haesner, M., Augustin, W., Scholl, S., Neu, T.R., Hempel, D.C., Horn, H., 2007. Structure and shear strength of microbial biofilms as determined with confocal laser scanning microscopy and fluid dynamic gauging using a novel rotating disc biofilm reactor. Biotechnol. Bioeng. 98, 747–755.

Morgenroth, E., Wilderer, P.A., 1999. Controlled biomass removal - the key parameter to achieve enhanced biological phosphorus removal in biofilm systems. Water Sci. Technol. 39 (7), 33–40.

Paramonova, E., Kalmykowa, O.J., Van Der Mei, H.C., Busscher, H.J., Sharma, P.K., 2009. Impact of hydrodynamics on oral biofilm strength. J. Dent. Res. 88, 922–926.

Peterson, B.W., van der Mei, H.C., Sjollema, J., Busscher, H.J., Sharma, P.K., 2013. A distinguishable role of eDNA in the viscoelastic relaxation of biofilms. mBio 4 (5) e00497-13.

Phani, K.K., Niyogi, S.K., 1987. Young's modulus of porous brittle solids. J. Mater. Sci. 22, 257–263.

Picioreanu, C., Van Loosdrecht, M.C.M., Heijnen, J.J., 2001. Two-dimensional model of biofilm detachment caused by internal stress from liquid flow. Biotechnol. Bioeng. 72, 205–218.

Radu, A.I., Vrouwenvelder, J.S., van Loosdrecht, M.C.M., Picioreanu, C., 2010. Modeling the effect of biofilm formation on reverse osmosis performance: flux, feed channel pressure drop and solute passage. J. Membr. Sci. 365, 1–15.

Ryshkewitch, E., 1953. Compression strength of porous sintered alumina and zirconia: 9th communication to ceramography. J. Am. Ceram. Soc. 36, 65–68.

Shaw, T., Winston, M., Rupp, C.J., Klapper, I., Stoodley, P., 2004. Commonality of elastic relaxation times in biofilms. Phys. Rev. Lett. 93, 98102.

Shen, Y., Huang, C., Monroy, G.L., Janjaroen, D., Derlon, N., Lin, J., Espinosa-Marzal, R., Morgenroth, E., Boppart, S.A., Ashbolt, N.J., Liu, W.-T., Nguyen, T.H., 2016. Response of simulated drinking water biofilm mechanical and structural properties to long-term disinfectant exposure. Environ. Sci. Technol. 50 (4), 1779–1787.

Stoodley, P., Jacobsen, A., Dunsmore, B.C., Purevdorj, B., Wilson, S., Lappin-Scott, H.M., Costerton, J.W., 2001. The influence of fluid shear and AlCl3 on the material properties of Pseudomonas aeruginosa PAO1 and Desulfovibrio sp. EX265 biofilms. Water Sci. Technol. 43 (6), 113–120.

Stoodley, P., Cargo, R., Rupp, C., Wilson, S., Klapper, I., 2002. Biofilm material properties as related to shear-induced deformation and detachment phenomena. J. Ind. Microbiol. Biotechnol. 29, 361–367.

Stoodley, P., Lewandowski, Z., Boyle, J.D., Lappin-Scott, H.M., 1999. Structural deformation of bacterial biofilms caused by short-term fluctuations in fluid shear: an in situ investigation of biofilm rheology. Biotechnol. Bioeng. 65, 83–92.

Taherzadeh, D., Picioreanu, C., Horn, H., 2012. Mass transfer enhancement in moving biofilm structures. Biophys. J. 102, 1483–1492.

Taherzadeh, D., Picioreanu, C., Küttler, U., Simone, A., Wall, W.A., Horn, H., 2010. Computational study of the drag and oscillatory movement of biofilm streamers in fast flows. Biotechnol. Bioeng. 105, 600–610.

Tierra, G., Pavissich, J.P., Nerenberg, R., Xu, Z., Alber, M.S., 2015. Multicomponent model of deformation and detachment of a biofilm under fluid flow. J. R. Soc. Interface 12, 1–13.

Towler, B.W., Cunningham, A., Stoodley, P., McKittrick, L., 2006. A model of fluid–biofilm interaction using a Burger material law. Biotechnol. Bioeng. 96 (2), 259–271.

Wagner, M., Taherzadeh, D., Haisch, C., Horn, H., 2010. Investigation of the mesoscale structure and volumetric features of biofilms using optical coherence tomography. Biotechnol. Bioeng. 107, 844–853.

Wagner, M., Horn, H., 2017. Optical coherence tomography in biofilm research: a comprehensive review. Biotechnol. Bioeng. 114 (7), 1386–1402.

Waters, M.S., Kundu, S., Lin, N.J., Lin-Gibson, S., 2014. Microstructure and mechanical properties of in situ Streptococcus mutans biofilms. ACS Appl. Mater. Interfaces 6 (1), 327–332.

Xi, C., Marks, D., Schlachter, S., Luo, W., Boppart, S., 2006. High-resolution three-dimensional imaging of biofilm development using optical coherence tomography. J. Biomed. Optic. 11, 34001.

Zhang, T.C., Bishop, P.L., 1994. Density, porosity, and pore structure of biofilms. Water Res. 28, 2267–2277.